Histone H3K27me3 demethylases regulate human Th17 cell development and effector functions by impacting on metabolism

Adam P. Cribbs[a,1], Stefan Terlecki-Zaniewicz[a], Martin Philpott[a], Jeroen Baardman[b], David Ahern[c], Morten Lindow[d], Susanna Obad[d], Henrik Oerum[d], Brante Sampey[e], Palwinder K. Mander[f], Henry Penn[g], Paul Wordsworth[a], Paul Bowness[a], Menno de Winther[h], Rab K. Prinjha[f], Marc Feldmann[a,c,1], and Udo Oppermann[a,i,j,k,1]

[a]Botnar Research Center, Nuffield Department of Orthopedics, Rheumatology and Musculoskeletal Sciences, National Institute for Health Research Oxford Biomedical Research Unit, University of Oxford, OX3 7LD Oxford, United Kingdom; [b]Experimental Vascular Biology, Department of Medical Biochemistry, Amsterdam Cardiovascular Sciences, Amsterdam University Medical Centres, University of Amsterdam, 1105AZ Amsterdam, The Netherlands; [c]Kennedy Institute of Rheumatology, Nuffield Department of Orthopedics, Rheumatology and Musculoskeletal Sciences, National Institute for Health Research Oxford Biomedical Research Unit, University of Oxford, OX3 7FY Oxford, United Kingdom; [d]Roche Innovation Center Copenhagen A/S, DK 2970 Hørsholm, Denmark; [e]Metabolon Inc., Durham, NC 27713; [f]Epinova Discovery Performance Unit, Medicines Research Centre, GlaxoSmithKline R&D, SG1 2NY Stevenage, United Kingdom; [g]Arthritis Centre, Northwick Park Hospital, HA13UJ Harrow, United Kingdom; [h]Institute for Cardiovascular Prevention, Ludwig Maximilians University, 80336 Munich, Germany; [i]Structural Genomics Consortium, University of Oxford, OX3 7DQ Oxford, United Kingdom; [j]Freiburg Institute for Advanced Studies, 79104 Freiburg, Germany; and [k]Oxford Centre for Translational Myeloma Research, Botnar Research Centre, University of Oxford, OX3 7LD Oxford, United Kingdom

Contributed by Marc Feldmann, January 26, 2020 (sent for review November 21, 2019; reviewed by Steffen Gay and John O'Shea)

T helper (Th) cells are CD4$^+$ effector T cells that play a critical role in immunity by shaping the inflammatory cytokine environment in a variety of physiological and pathological situations. Using a combined chemico-genetic approach, we identify histone H3K27 demethylases KDM6A and KDM6B as central regulators of human Th subsets. The prototypic KDM6 inhibitor GSK-J4 increases genome-wide levels of the repressive H3K27me3 chromatin mark and leads to suppression of the key transcription factor RORγt during Th17 differentiation. In mature Th17 cells, GSK-J4 induces an altered transcriptional program with a profound metabolic reprogramming and concomitant suppression of IL-17 cytokine levels and reduced proliferation. Single-cell analysis reveals a specific shift from highly inflammatory cell subsets toward a resting state upon demethylase inhibition. The root cause of the observed antiinflammatory phenotype in stimulated Th17 cells is reduced expression of key metabolic transcription factors, such as PPRC1. Overall, this leads to reduced mitochondrial biogenesis, resulting in a metabolic switch with concomitant antiinflammatory effects. These data are consistent with an effect of GSK-J4 on Th17 T cell differentiation pathways directly related to proliferation and include regulation of effector cytokine profiles. This suggests that inhibiting KDM6 demethylases may be an effective, even in the short term, therapeutic target for autoimmune diseases, including ankylosing spondylitis.

Th17 cells | epigenetics | histone demethylase | metabolism | inflammation

Upon activation, naive CD4$^+$ T cells undergo differentiation into different types of T helper cells, including T helper 1 (Th1), Th2, and Th17, each characterized by different cytokine profiles and effector functions (1). In addition to their role as potent inducers of tissue inflammation, Th17 cells also serve physiological roles in host defense against bacterial or fungal infections and provide key roles in maintaining tissue barrier homeostasis (2–5). Transforming growth factor beta (TGF-β) and interleukin 6 (IL-6) are cytokines pivotal in the initial commitment of naive T cells toward the Th17 lineage (6–8), supported by other cytokines, such as IL-23, IL-21, and IL-1β, involved in the expansion, stability, and function of Th17 cells (9–11). The master transcriptional regulator RAR-related orphan receptor gamma (RORγt) is necessary to coordinate the Th17 commitment and promotes IL-17 expression (12). A loss or inhibition of RORγt can block Th17 differentiation in vitro and is inhibitory in models of autoimmune encephalomyelitis, imiquimod-induced cutaneous inflammation, and collagen-induced arthritis (13–15).

The critical role of epigenome and chromatin modifications in differentiation and commitment from naive T cells to T helper subsets has been demonstrated (16, 17). Chromatin-templated posttranslational modifications control gene transcription, DNA replication, and DNA repair, resulting in the concept of a "chromatin code" or "histone code" that determines distinct cell states

Significance

T cells control many immune functions, with Th17 cells critical in regulating inflammation. Following activation, T cells undergo metabolic reprogramming and utilize glycolysis to increase the ATP availability. Epigenetic mechanisms controlling metabolic functions in T cells are currently not well-defined. Here, we establish an epigenetic link between the histone H3K27me3 demethylases KDM6A/B and the coordination of a metabolic response. Inhibition of KDM6A/B leads to global increases in the repressive H3K27me3 histone mark, resulting in down-regulation of key transcription factors, followed by metabolic reprogramming and anergy. This work suggests a critical role of H3K27 demethylase enzymes in maintaining Th17 functions by controlling metabolic switches. Short-term treatment with KDM6 enzyme inhibitors may be useful in the therapy of chronic inflammatory diseases.

Author contributions: A.P.C., M.F., and U.O. designed research; A.P.C., S.T.-Z., M.P., J.B., D.A., B.S., H.P., P.W., P.B., and M.d.W. performed research; M.L., S.O., H.O., P.K.M., R.K.P., and U.O. contributed new reagents/analytic tools; A.P.C., B.S., and U.O. analyzed data; A.P.C., M.F., and U.O. wrote the paper; and H.P., P.W., and P.B. provided patient samples.

Reviewers: S.G., Center of Experimental Rheumatology; and J.O., National Institutes of Health.

Competing interest statement: B.S. was an employee of Metabolon. P.K.M. and R.K.P. are employees of GlaxoSmithKline. M.L., S.O., and H.O. were at Roche. U.O. and S.G. are coauthors on a 2016 meeting report.

Data deposition: Single-cell RNA-seq, RNA-seq, ATAC-seq, and ChIP-seq datasets are deposited with the Gene Expression Omnibus (GEO) database under accession no. GSE127767. A computational pipeline was written employing scripts from the Computational Genomics Analysis Toolkit (CGAT) (84, 86) to analyze the next generation sequencing data (https://github.com/cgat-developers/cgat-flow). R scripts used for transcriptomic data analysis are available through GitHub (https://github.com/Acribbs/deseq2_report).

[1]To whom correspondence may be addressed. Email: adam.cribbs@imm.ox.ac.uk, marc.feldmann@kennedy.ox.ac.uk, or udo.oppermann@sgc.ox.ac.uk.

This article contains supporting information online at https://www.pnas.org/lookup/suppl/doi:10.1073/pnas.1919893117/-/DCSupplemental.

First published March 2, 2020.

(18). In this context, methylation of histone arginyl and lysyl residues plays a fundamental role in the maintenance of both active and suppressed states of gene expression, depending on the precise sites and the degree of methylation (19). The trithorax and polycomb paradigms, in particular, identified in *Drosophila* genetics are centered around trimethylation of histone H3 at lysine residue position 4, (H3K4me3), which is correlated with active transcription, and trimethylation of lysine 27 in histone H3 (H3K27me3), which is associated with repression of gene transcription. The reversibility and dynamic behavior of H3K27 methylation is provided by the methyltransferase *enhancer of zeste homolog 2* (EZH2) and by several members of the Jumonji domain containing (Jmj) $Fe2^+$ and 2-ketoglutarate dependent oxygenases, which catalyze demethylation of methylated histone lysine residues in vitro and in vivo. In particular, ubiquitously transcribed tetratricopeptide repeat gene, X chromosome (or UTX, KDM6A) and Jmj family members 3 (or JMJD3, KDM6B) are documented specific histone H3K27me2/3 demethylases.

Global analysis of histone modifications and DNA methylation in different T cell subsets has led to a better understanding of the mechanisms controlling differentiation and plasticity crucial for the function of T helper subsets (17, 20, 21). Integrated analysis of epigenomic profiles supports a linear model of memory differentiation where epigenetic mechanisms control the activation of fate-determining transcription factors (17). A limited number of studies have investigated the epigenetic mechanisms involved in regulating Th17 differentiation and function. Hypomethylation of DNA cytosine residues in Th17-specific genes IL17A and RORC shows a strong correlation with differentiation and the activation of effector function (22). Global mapping of H3K4me3 and H3K27me3 histone marks has revealed that chromatin modifications also contribute to the specificity and plasticity of effector Th17 cells and provides a framework for using global epigenomic analyses to understand the complexity of T helper cell differentiation (23). Subsequently, chemical screening using inhibitors against various components of the epigenetic machinery has revealed novel epigenetic pathways that regulate Th17 effector function. These include the BET bromodomains, the CBP/p300 bromodomain, and the KDM6A/KDM6B Jumonji histone demethylases, able to regulate $CD4^+$ differentiation or Th17 function in vitro (24–27).

Metabolic pathways are intimately linked with epigenetics and transcriptional regulation and modulate cell fate and function (28–31). Moreover, targeting metabolic pathways with small molecules in autoimmunity may be a beneficial strategy for the treatment of Th17-mediated disease, such as ankylosing spondylitis (AS). For example, it has been reported that metabolic reprogramming using the small molecule aminooxy-acetic acid is sufficient to shift the differentiation of Th17 cells toward an inducible regulatory T cell (iTreg) phenotype, involving accumulation of 2-hydroxyglutarate, leading to hypomethylation of the gene locus of the key Treg transcription factor *foxp3* (32).

Here, we establish a link between the H3K27 demethylases KDM6A and KDM6B in regulating Th17 cell metabolism. We show that KDM6A and KDM6B demethylases are key factors in regulating the Th17 proinflammatory phenotype and control metabolic function and differentiation into effector cells. Inhibiting these enzymes results in a global increase in H3K27me3, with consequential metabolic reprogramming that leads to the emergence of an anergic phenotype, a state that should be useful in ameliorating disease.

Results

Inhibitor Screening Identifies Histone H3K27 Demethylases as Key Regulators of Proinflammatory Effector T Cell Phenotypes. Using a focused library of small molecule inhibitors (*SI Appendix*) that target eight major classes of chromatin and epigenetic proteins, we measured the expression of Th cytokines following 24 h of treatment of in vitro differentiated $CD4^+$ cells. We evaluated the expression of interferon-γ (IFN-γ), IL-4, and IL-17 as markers for Th1, Th2, and Th17 cells, respectively (Fig. 1*A*). A consistent down-regulation of cytokine expression following treatment with inhibitors against the JmjC domain-containing histone demethylases (KDM6A/KDM6B), bromodomains, and histone deacetylases (HDACs) was observed in all effector subsets (Fig. 1*A* and *SI Appendix*, Fig. S1*A*), suggesting a common epigenetic susceptibility. Given the importance of H3K27 (KDM6) demethylases in cellular development (33, 34) and inflammation (35), we focused this study toward the prototypic KDM6 inhibitor GSK-J4 (36), displaying an EC_{50} of 2 μM (*SI Appendix*, Fig. S1*B*), and its inactive regional isomer GSK-J5 as a control. Using two different Th17 differentiation models, in which either $CD4^+$ or $CD45RA^+$ cells are cultured in a mixture of IL-6, IL-23, and TGF-β cytokines for 7 d, followed by treatment with dimethyl sulfoxide (DMSO), GSK-J4, or GSK-J5 for 48 h, we observed a significant reduction in IL-17 and IFN-γ (Fig. 1*B* and *SI Appendix*, Fig. S2*A*) by GSK-J4, with constant levels of RORC expression (*SI Appendix*, Fig. S2*A*). In contrast, addition of GSK-J4 during the differentiation process led to reduced cytokine production (*SI Appendix*, Fig. S2 *B* and *C*), with a significant reduction in the expression of RORC (*SI Appendix*, Fig. S2*C*), indicating that this Th17 master transcription factor requires KDM6 demethylase activity during differentiation and not in the effector state.

Histone Demethylases KDM6A and KDM6B Regulate Th17 Cell Maturation. We observed a decrease in the activation of Th17 cells, as measured by CD25 and CCR4 flow cytometry staining, following culture in the presence of GSK-J4 (*SI Appendix*, Fig. S2 *D* and *E*). No increase in cell death was measured following 48 h of GSK-J4 treatment, as measured by propidium iodide and Annexin-V staining (*SI Appendix*, Fig. S2*F*). GSK-J4 is a cell-permeable and potent selective inhibitor of KDM6 demethylases and has approximately fivefold to 20-fold lower activity against KDM5B demethylating enzymes in vitro (36, 37). In order to assess the specificity of GSK-J4 and evaluate the contribution of each KDM enzyme to Th17 function, we used locked nucleic acid (LNA) knockdown of KDM6A/B and the potential GSK-J4 off-target, KDM5B (JARID1B) (Fig. 1*C*). Knockdown of KDM6A and KDM6B, either against single or simultaneously against both targets, led to reduced levels of IL-17 and IFN-γ (Fig. 1*D* and *SI Appendix*, Fig. S3 *A* and *B*). Moreover, knockdown of KDM6A and KDM6B also impacted on the proliferation of Th17 cells, as measured by cell counting (Fig. 1*E*), whereas KDM5B knockdown had a lesser impact on these phenotypes. The results corroborate the role for Jumonji histone demethylase activity regulating the proinflammatory function and proliferation of Th17 cells (27, 38) and confirm the previously noted KDM6A/B on-target activity of the GSK-J4 chemical tool compound (36).

KDM6 Inhibitor Treatment Suppresses Proinflammatory Cytokine Production and Proliferation in Autoimmune Patient Cells. It was of interest to validate the earlier antiinflammatory observations within a context of chronic inflammation. Consistent with our earlier work on chronic inflammation in natural killer (NK) cells (35), we observed IFN-γ reduction in GSK-J4–treated $CD3^+$ T cells isolated from rheumatoid arthritis (RA) patients (Fig. 2*A*), and also of IL-17 in AS patients (Fig. 2*B*). A significant reduction in the proportion of cells in G2/M phase (Fig. 2*C*), associated with reduced Th17 proliferation following treatment with GSK-J4 (Fig. 2*D*), was observed. The reversible nature of the GSK-J4 effect was demonstrated in washout experiments where cells were treated for 48 h with the inhibitor, followed by media change after 24 h where GSK-J4 was omitted. After 48 h, cells partially regained their ability to secrete cytokines (Fig. 2*E*). Single-cell profiling using mass cytometry (CyTOF) allowed deep immune phenotyping and analysis of cell cycle progression of Th cells enriched from AS

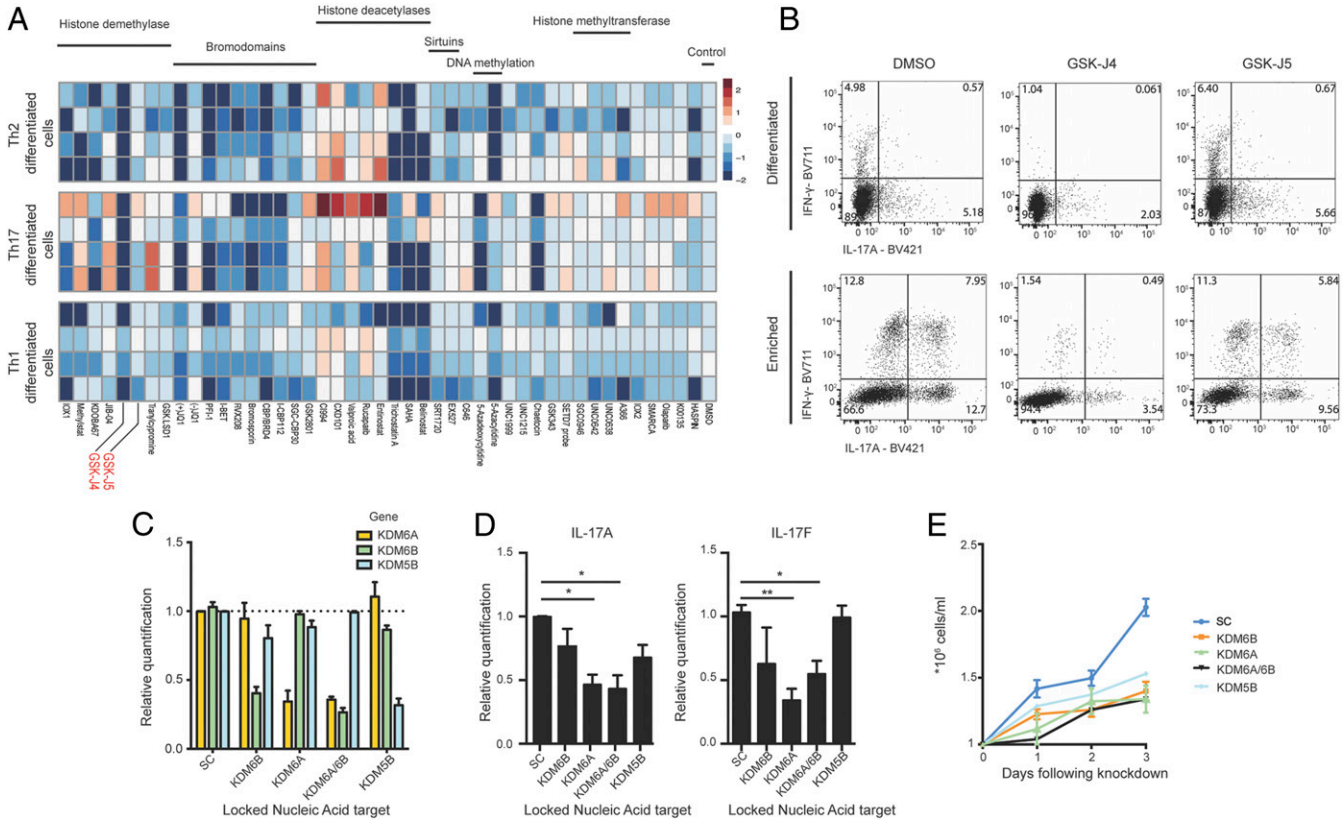

Fig. 1. Small-molecule inhibitor screening identifies KDM6A and KDM6B as key regulators of Th17 function. (*A*) Heat map reporting as Log2 fold change the secretion levels of IL-4, IL-17, and IFNγ from CD45RA$^+$ T cells differentiated in Th2, Th17, and Th1 polarizing conditions. Cytokine expression was measured by ELISA following 24 h of culture with a library of small-molecule epigenetic inhibitors. (*B*) Flow cytometric analysis of IL-17 and IFN-γ staining for Th17 differentiated cells treated with DMSO, GSK-J4, or GSK-J5. (*C*) The mRNA expression as measured by real-time PCR following 7 d of locked nucleic acid (LNA) knockdown of GSK-J4 targets, KDM6A, KDM6B, and KDM5B. Data represent mean ± SEM ($n = 3$). Scrambled control (SC) LNA was used as a control. (*D*) Real-time PCR quantification of IL-17A and IL-17F following LNA knockdown of KDM6A, KDM6B dual knockdown KDM6A/KDM6B, or KDM5B. (*E*) SC LNA in Th17 differentiated cells over 3 d of culture. *P* values were calculated using a Mann–Whitney *U* test. *$P < 0.05$, **$P < 0.01$. Error bars show mean ± SD.

patients in response to GSK-J4 treatment. The t-distributed stochastic neighbor embedding (t-SNE) plots (*SI Appendix*, Fig. S4*A*) confirm that GSK-J4 has a broad antiinflammatory effect (35, 36, 39), highlighting a reduction in TNFα, IL-22, and IL-17 cytokines (*SI Appendix*, Fig. S4*B*). Activation markers, such as HLA-DR and CD25, were found to be reduced following treatment with GSK-J4, in addition to a reduction in cell proliferation marker Ki-67 (*SI Appendix*, Fig. S4*C*). Interestingly, we observed an up-regulation of CXCR3, CCR7, and CD3 surface marker expression following GSK-J4 treatment, suggesting an increase in activated and/or memory T cells (*SI Appendix*, Fig. S4*C*) To identify cell cycle clusters, we manually gated based on the expression of phospho-histone H3 (P-histone, Ser10), IDU, and pRb, representing markers of cell cycle progression (Fig. 2 *F* and *G*). This confirms a reduction in S phase and an increase in cells in G0 phase. Combined, these data suggest that GSK-J4 induces a reversible anergic state in human Th17 cells.

Histone Demethylase Treatment Induces Transcriptional Changes Affecting Immune Phenotype and Metabolism of Th17 Cells. To understand the GSK-J4–mediated phenotypic changes, we initially analyzed gene expression using bulk RNA sequencing (RNA-seq) (Dataset S1), performed in CD4$^+$ T cells enriched for 7 d in IL-6, IL-23, and TGF-β, and then cultured in the presence of GSK-J4 or DMSO for 24 h. These data reveal a transcriptional signature that comprises >2,200 genes with a significant log2-fold change and with ∼58% showing down-regulation (Fig. 3*A*). Reactome pathway analysis of differentially regulated genes showed that GSK-J4 impacts on processes comprising metabolic pathways, cell cycle, respiratory chain electron transport, and interleukin and cytokine signaling (Fig. 3*B* and *SI Appendix*, Fig. S5*A*) and, in addition, shows up-regulation of ATF4 and DDIT3, indicating a possible ATF4-mediated stress response. Although ATF4 and DDIT3 (CHOP) are up-regulated, confirmed by qPCR (Fig. 3*D*), typical downstream metabolic targets, including, for example, argininosuccinate synthase (ASS1) or asparagine synthase (ASNS) (Fig. 3*C*) are not significantly affected. Knockdown of KDM6B, but not KDM6A or KDM5B, revealed a similar ATF4 transcriptional response (Fig. 3*E*) as GSK-J4, confirming that this effect is specifically driven by inhibition of KDM6B histone demethylase activity. Downstream ATF4/DDIT3 effects do not appear to be regulated through the canonical stress-induced eIF2α phosphorylation pathway since ISRIB (40), a generic inhibitor of the ATF4-mediated integrated stress response (ISR), did not result in cytokine levels similar to control conditions (Fig. 3*F*) and possibly explains the lack of induction of classical stress-induced metabolic ATF4 targets. Next, we examined the global levels of H3K27me3, the KDM6 demethylase substrate, in addition to H3K4me3. We identified substantial global increases in H3K27me3 at transcriptional start sites (TSSs) upon GSK-J4 inhibition, consistent with the expected effect of KDM6A/KDM6B as H3K27 demethylases (Fig. 3*G*). In line with a large fraction of up-regulated genes, we also observed global increases in H3K4me3 at TSSs following GSK-J4 treatment (Fig. 3*H*). The change in H3K27me3 was greater in genes that showed the largest down-regulation (Fig. 3*I*), supporting a model of polycomb repressive

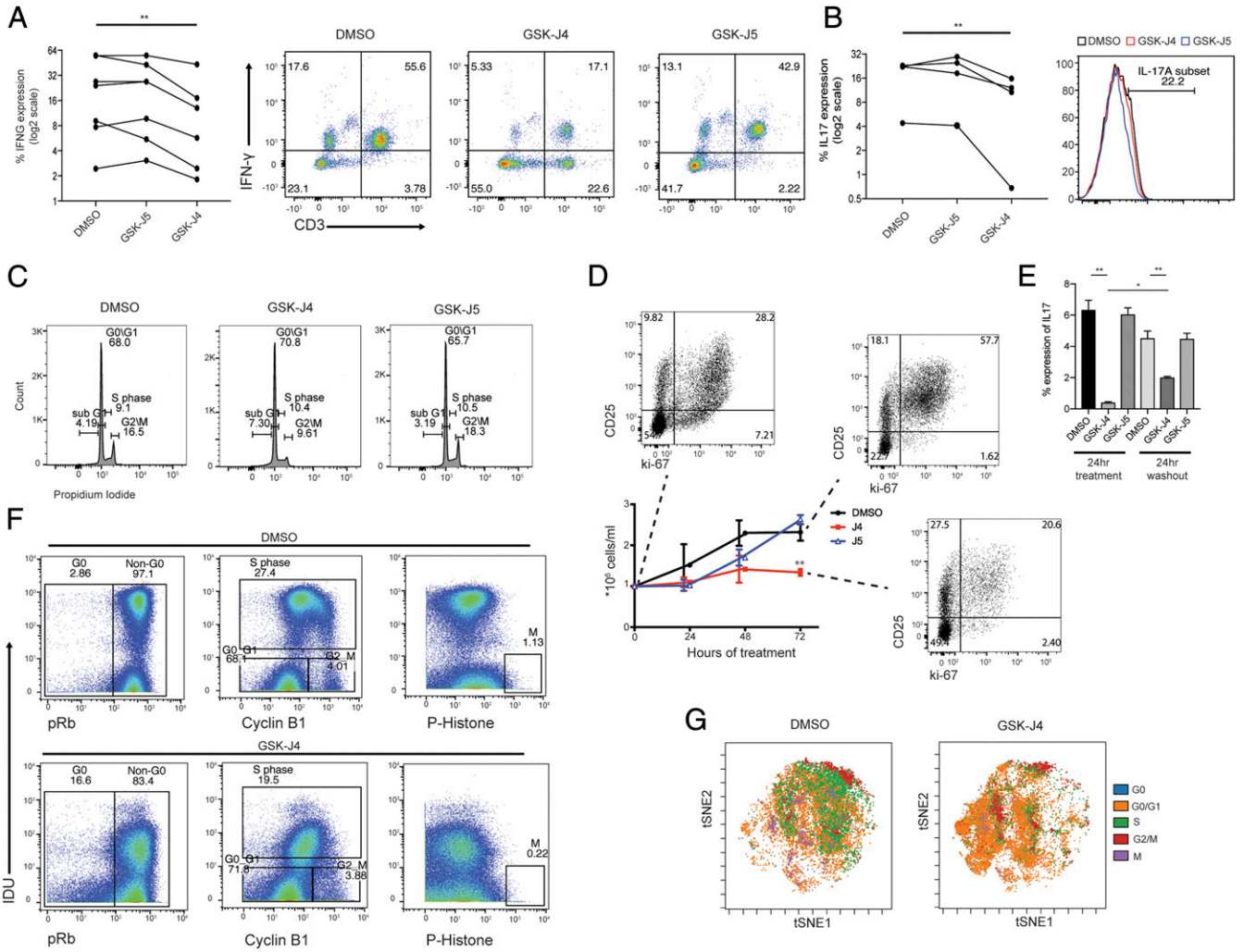

Fig. 2. KDM6A and KDM6B regulate Th17 proinflammatory function in both acute and chronic inflammatory disease. (*A*) Flow cytometric evaluation of IFNγ expression in $CD3^+$ T cells isolated from rheumatoid arthritis patients. Cells were treated with DMSO, GSK-J4, or GSK-J5 and stimulated for 4 h with PMA/ionomycin in the presence of protein transport inhibitor for the last 3 h of culture ($n = 7$). (*Left*) Shows the percent expression of IFNγ. (*Right*) Shows representative flow cytometry plots. (*B*) Flow cytometric evaluation of IL-17 expression in $CD4^+$ T cells isolated from ankylosing spondylitis patients. (*C*) Cell cycle evaluation using propidium iodide (PI) staining following 24 h of DMSO, GSK-J4, or GSK-J5 treatment. The numbers in each gate represent the percent of cells in each phase of cell cycle. (*D*) Cell counting following 72 h of culture with DMSO, GSK-J4, or GSK-J5. Flow cytometric analysis shows the expression of Ki-67 and CD25. (*E*) Th17 differentiated cells were treated with DMSO, GSK-J4, or GSK-J5 for 24 h, and then cells were washed three times and cultured for a further 24 h. Expression of IL17 was measured by flow cytometry. (*F*) Representative example of cell cycle markers measured using CyTOF following 24 h of treatment with (*Bottom*) GSK-J4 or (*Top*) DMSO. (*G*) tSNE clustering showing cell cycle stages identified by the gating strategy shown in *F*. All flow cytometry and CyTOF experiments were representative of $n = 3$ independent experiments. *P* values were calculated using Wilcoxon matched pairs test. $*P < 0.05$, $**P < 0.01$. Error bars show mean ± SD.

complex (PRC)-mediated gene silencing. However, several upregulated genes, such as DDIT3, show inverse patterns, such as increased levels of repressive H3K27 marks with reduced H3K4me3 levels (Fig. 3*J*), whereas the T-box transcription factor Tbet (TBX21) regulating T cell functions and being a direct, repressed target of DDIT3 (41), follows a pattern of PRC-mediated silencing with increased H3K27me3 levels and reduced H3K4me3 and transcript levels (Fig. 3*K*).

Single-Cell Transcriptomics Reveals Distinct Populations of Inflammatory T Cells Following KDM6 Inhibition. The observation of extensive heterogeneity with respect to cell cycle progression (Fig. 2) prompted us to evaluate metabolic or immune gene expression by using single-cell transcriptomics (Dataset S2). We initially performed single-cell analysis on peripheral blood mononuclear cell (PBMC) samples cultured in the presence of either DMSO or GSK-J4 and observed a general antiinflammatory response in all major cell types exposed to GSK-J4 (*SI Appendix*, Fig. S6*A*). $CD4^+$ T cells were then isolated from AS patients and enriched for 7 d in IL-6, IL-23, and TGF-β, followed by 24-h treatment with DMSO or GSK-J4. Single-cell transcriptome analysis was then performed on ∼2,000 cells from each donor ($n = 3$ donors) (Fig. 4*A*). We identified nine unique clusters based on their gene expression profiles, comparable across all three patients (Fig. 4*B* and *SI Appendix*, Fig. S6 *B* and *C*). Similar to the mass cytometry data, we observed a significant shift in the t-SNE clustering following GSK-J4 treatment, with reduced numbers of cells within clusters 1, 2, 4, 8, and 9 and increased numbers of cells within clusters 3, 5, 6, and 7 (Fig. 4*B*). Clusters 1 and 3 showed the strongest expression of inflammatory cytokines, such as IFN-γ and IL-17A (Fig. 4*C* and *SI Appendix*, Fig. S6*D*), and displayed a strong shift in cell numbers following treatment with GSK-J4. In agreement with our bulk RNA-seq data, we also observed a significant increase

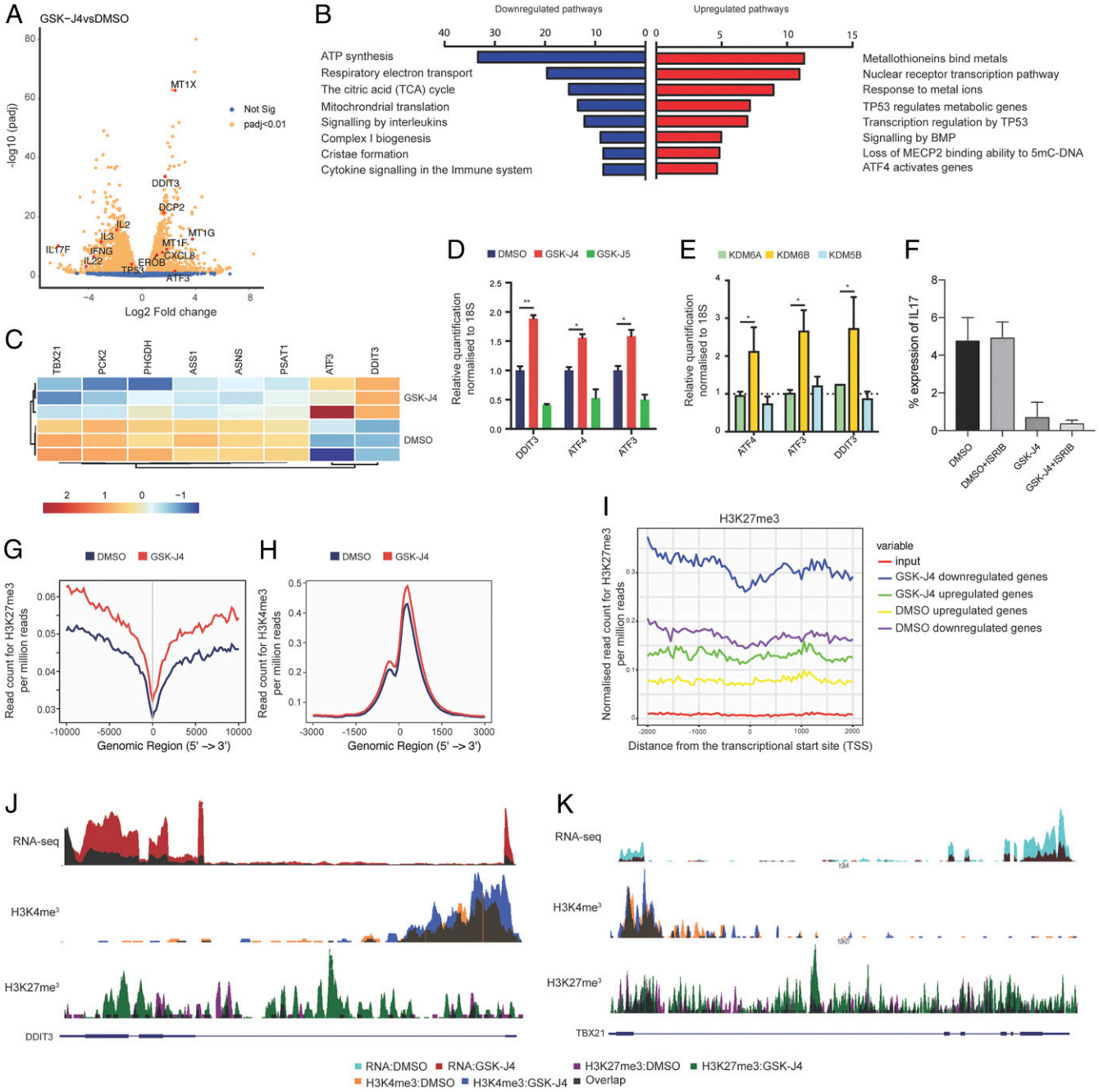

Fig. 3. KDM6A/KDM6B inhibition induces a transcriptional change that affects immune metabolic function. (*A*) Volcano plot showing selected gene differential expression. (*B*) GO analysis showing the top down-regulated and up-regulated ontology enrichment analysis. (*C*) Heat map displaying the transcriptional response of genes associated with metabolic function. (*D*) RT-qPCR analysis of Th17 differentiated cells treated for 24 h with DMSO, GSK-J4, or GSK-J5. (*E*) RT-qPCR analysis of Th17 differentiated cells treated for 7 d with LNAs targeting KDM6A, KDM6B, or KDM5B. (*F*) Th17 differentiated cells were treated for 24 h with DMSO, GSK-J4 in the presence of absence of ISRIB. IL-17A cytokine expression was measured by flow cytometry. (*G*) Coverage plot showing the H3K27me3 read count per million collapsed around the TSS of all genes following treatment with DMSO or GSK-J4. (*H*) Coverage plot showing the H3K4me3 read count per million collapsed around the TSS of all genes following treatment with DMSO or GSK-J4. (*I*) Correlation of up-regulated and down-regulated genes from RNA-seq dataset with the H3K27me3 read count per million collapsed around the TSS. A coverage plot highlighting the H3K27me3 read count per million separated by up-regulated and down-regulated genes following Th17 cell treatment with either DMSO or GSK-J4. (*J*) Genome browser view of the DDIT3 gene showing RNA-seq and the enrichment of H3K4me3 and H3K27me3 in cells treated with either DMSO or GSK-J4. (*K*) Genome browser view similar to *J* for TBX21 gene. *P* values were calculated for *D* and *E* using a Mann–Whitney *U* test. Error bars show mean ± SD. $*P < 0.05$, $**P < 0.01$.

in DDIT3 expression following GSK-J4 treatment (Fig. 4*D*). We identified discriminatory markers that account for the shift in T cell clustering in response to GSK-J4 for each of the clusters (Fig. 4*E*). Clusters 1, 4, 8, and 9 were associated with a robust inflammatory signature, with enrichment of cytokines, such as IL-26, IL-17A, IL-17F, and IFN-γ (Fig. 4 *C* and *E* and *SI Appendix*, Fig. S6*D*). In contrast, clusters 5 and 7, which were nearly absent in the DMSO treatment, were primarily associated with an increase in cell numbers following GSK-J4 treatment and showed a metallothionein gene enrichment and an ATF4 response (*SI Appendix*, Fig. S6 *E* and *F*).

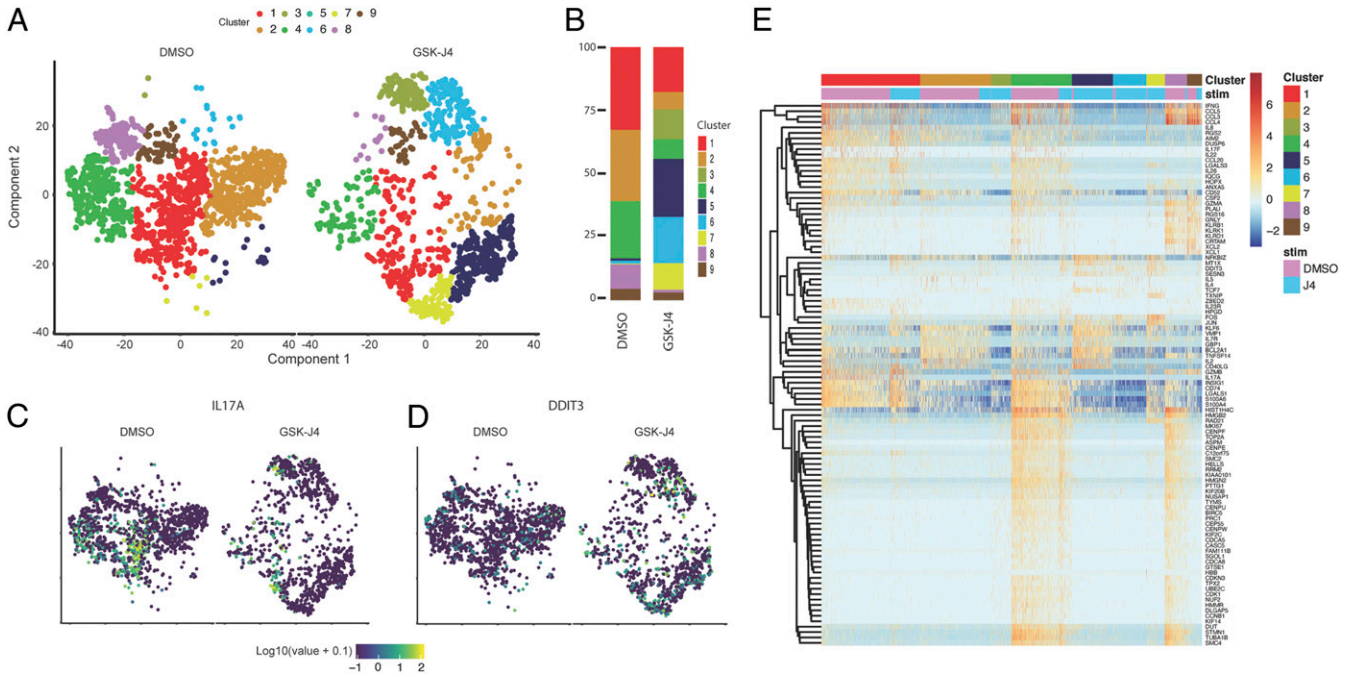

Fig. 4. Single-cell transcriptomics identifies a complex T cell response to KDM6A/KDM6B inhibition. (*A*) tSNE plot showing clustering of CD4$^+$ T cells isolated from AS patients cultured in Th17 promoting cytokines. (*Left*) Shows cells cultured for 24 h in DMSO. (*Right*) Shows the cells following GSK-J4 treatment. (*B*) Plot showing the proportion of each cluster in both treatment groups. (*C*) tSNE plot showing the expression of IL-17A expression. (*D*) tSNE plot showing expression of DDIT3. (*E*) Heat map showing the cluster-specific markers for each population.

Clusters 8 and 9 produced high levels of chemokines, with cluster 8 expressing high levels of proliferative markers, such as MKI67 (Ki-67) (*SI Appendix*, Fig. S6*G*). Cluster 7, which is almost exclusively expressed following GSK-J4 treatment, showed high expression of T cell memory markers, such as PTPRC (CD45) and CCR7, indicating a shift from proliferating or inflammatory cells toward a memory or resting phenotype (Fig. 4*E* and *SI Appendix*, Fig. S6*H*). To further investigate the complex pattern of T cell differentiation in response to GSK-J4, we performed pseudotemporal ordering to identify genes that are differentially regulated as a component of T cell differentiation. By using a semisupervised method, where genes associated with the Gene Ontology (GO) term "T cell activation" (GO:0042110), we defined the biological trajectory (42). DMSO-treated and GSK-J4–treated cells are placed at opposite ends of the pseudotime trajectory (*SI Appendix*, Fig. S7*A*), confirming that GSK-J4 treatment leads to a significant reduction in genes associated with T cell activation. This approach also identified a significant number of genes associated with the tricarboxylic acid (TCA) cycle and the electron transport chain that were down-regulated as a consequence of GSK-J4 treatment (*SI Appendix*, Fig. S7*B*).

GSK-J4 Induces Metabolic Reprogramming in Th17 Cells. The observed transcriptomic changes suggested a link between H3K27 demethylase inhibitor treatment and metabolic perturbations, leading us to investigate in more detail the resulting T cell metabolome (Dataset S3). Human CD45RA$^+$ T cells were isolated from six healthy donors, and Th17 cells were obtained as described above and treated with DMSO, GSK-J4, and its negative control GSK-J5. Extracts taken at 12-h and 24-h time points were subjected to a liquid chromatography-mass spectrometry (LC-MS)-based approach. Random Forest comparisons produced predictive accuracies of 83.3% or greater (DMSO vs. GSK-J4 vs. GSK-J5) (*SI Appendix*, Fig. S8*A*), which is well above what would be expected from random chance alone (33% for a three-way comparison). Cellular metabolite changes during the Th17 differentiation process indicated a notable shift toward glucose utilization, increased pentose phosphate pathway (PPP) metabolism, and a marked increase in the nucleotides, such as nicotinamide adenine dinucleotide (NAD^+), flavin adenine dinucleotide (FAD), and adenosine diphosphate (ADP) ribose levels (Fig. 5*A* and *SI Appendix*, Figs. S8 and S9). Depletion of several amino acids, cellular ascorbate, and a strong signature of membrane lipid biosynthesis, as well as an increase in protein glycosylation pathway activity (*SI Appendix*, Fig. S9), were also observed. These cellular profile changes are consistent with previously noted concomitant increases in both Th17 cellular proliferation and differentiation toward effector cytokine production (26). Treatment with GSK-J4, but not DMSO or GSK-J5, induced significant changes in metabolic pathways. Elevations in 3-phosphoglycerate and phosphoenolpyruvate (Fig. 5*B* and *SI Appendix*, Fig. S8) show that GSK-J4 increases glucose utilization at 24 h whereas ribose-5-phosphate and ribulose/xylulose 5-phosphate intermediates of the pentose phosphate pathway (PPP), shown to be activated with Th17 differentiation (43), were decreased following GSK-J4 treatment (Fig. 5*B* and *SI Appendix*, Fig. S8). Decreased PPP activity would be anticipated to have multiple biological impacts on Th17 cells, including diminished NADPH production and redox status or decreased nucleotide biosynthesis, as evidenced by significant reduced levels in multiple nucleotide metabolites (*SI Appendix*, Fig. S9*B*). A significant decrease in several fatty acid (propionylcarnitine, carnitine, deoxycarnitine) or branched chain amino acid metabolism intermediates was noted for GSK-J4 treatment at 12 and 24 h (Fig. 5*B* and Dataset S3). The metabolite changes agree with the observed transcriptional changes [e.g., increased expression of glucose transporters and glycolytic key enzymes, such as phosphofructokinase/bisphosphatase or lactate dehydrogenase (Fig. 5*C*)], explaining the increase in glycolytic activity. Conversely, down-regulation of key PPP enzymes, such as glucose-6-phosphate dehydrogenase (G6PD) or phosphogluconate dehydrogenase (PGD), explains the decreased flux through PPP whereas increased levels of pyruvate dehydrogenase kinase

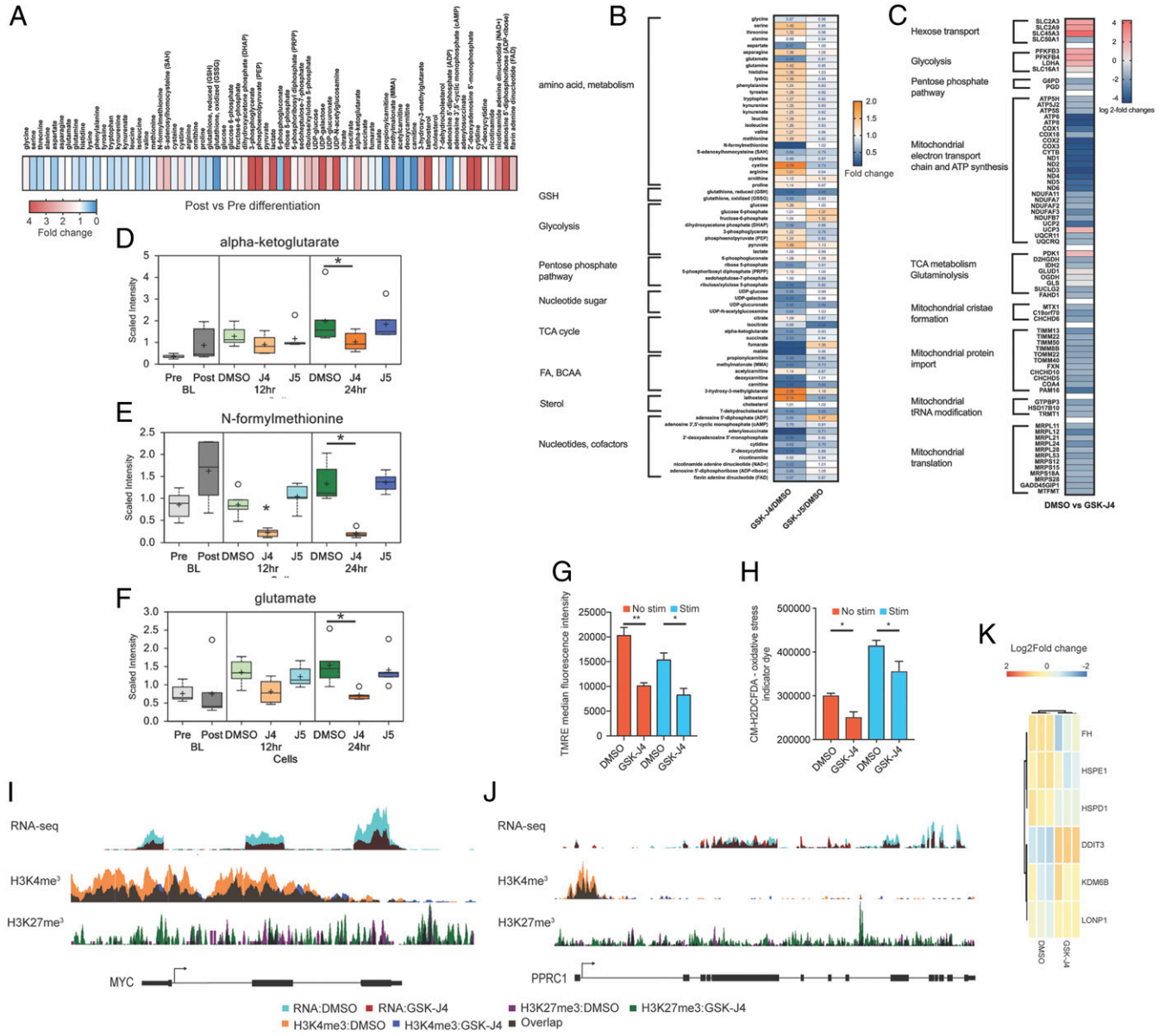

Fig. 5. Inhibition of KDM6A/B leads to metabolic reprogramming of Th17 cells. (*A*) Heat map showing the metabolite changes between predifferentiation and postdifferentiation. (*B*) Heat map showing the expression of selected metabolites grouped into functional classes in Th17 differentiated cells treated with either DMSO and GSK-J4 for 24 h. GSH, glutathione; FA, fatty acid; BCAA, branched-chain amino acid. (*C*) Heat map displaying the transcriptional response of genes associated with mitochondrial metabolic regulation and function. Box plots showing the scaled intensity of (*D*) α-ketoglutarate, (*E*) *N*-formylmethionine, and (*F*) glutamate from Th17 differentiated cells treated with DMSO, GSK-J4, and GSK-J5 for 24 h. BL, base line. (*G*) Mitochondrial membrane potential and (*H*) oxidative stress marker measurements following DMSO or GSK-J4 treatment of Th17 differentiated cells. (*I*) Genome browser view of the MYC gene showing RNA-seq and the enrichment of H3K4me3 and H3K27me3 in cells treated with either DMSO or GSK-J4. (*J*) Genome browser view similar to *F* for PPRC1 gene. (*K*) Heat map showing the expression of several genes involved in the UPR response pathway. *P* values were calculated using a Mann–Whitney *U* test. $*P < 0.05$, $**P < 0.01$. Error bars show mean ± SEM.

(PDK1) suggest reduction of glycolytic intermediates into the TCA cycle. Indeed, a uniquely observed effect with GSK-J4 treatment at both time points was a significant decrease in the TCA cycle metabolites α-ketoglutarate (α-KG), succinate, fumarate, and malate, with increased levels of glutamine and reduced glutamate (Fig. 5 *B*–*F*). This suggested that alterations in α-KG-dehydrogenase or changes in glutaminolysis that feed into the TCA cycle at the level of α-KG are related to the inhibitor-mediated decrease in α-KG. However, inspection of metabolite levels revealed that GSK-J4 reduces those TCA metabolites to a similar level as seen before differentiation (*SI Appendix*, Fig. S8*B*). Furthermore, no transcriptional changes in a-ketoglutarate dehydrogenase (OGDH), glutamate dehydrogenase (GLUD1), or glutaminase (GLS) were observed (Fig. 5*C*). This suggests that the reduction in TCA cycle metabolites reflects a general decrease in mitochondrial function and biogenesis. Indeed, this hypothesis is supported by reduced transcription of genes involved in electron transport, TCA cycle, cristae formation, protein import, mitochondrial tRNA metabolism, or protein translation (Fig. 5*C*), the latter also corroborated by reduction in levels of *N*-formylmethionine, a mitochondrial protein building block (Fig. 5*B*). Reduced mitochondrial activity was also observed by tetramethylrhodamine-ethyl ester (TMRE) staining, a measure of mitochondrial membrane potential (Fig. 5*G*), and a concomitant

reduction of reactive oxygen species (ROS) levels following GSK-J4 treatment (Fig. 5*H*). These wide-ranging mitochondrial impairments are likely related to silencing of key transcriptional regulators of mitochondrial and nuclear encoded mitochondrial genes, including c-MYC, PPARGC1a, and PPRC1 (Fig. 5 *I* and *J*). Importantly, we did not observe a transcriptional response of marker genes that would indicate a mitochondrial unfolded protein response (UPR^{mt}) (Fig. 5*K* and ref. 44).

Discussion

This work provides several insights into epigenetic control of Th17 cell functions. Consistent with previous studies highlighting the importance of histone demethylases KDM6A/B in cellular development and disease (45–48), we here extend previous observations that these enzymes are critical regulators of Th17 development and proinflammatory phenotypes. In murine $CD4^+$ T cells, KDM6B ablation promotes $CD4^+$ T cell differentiation into Th2 and Th17 subsets in small intestine and colon (26, 49); however, two other independent studies did not observe this enhanced Th17 differentiation in KDM6B-ablated $CD4^+$ T cells (26, 27, 38) but showed significant impairment of Th17 differentiation and effector function. One possible explanation for this discrepancy may be related to redundant and compensatory roles of KDM6A and KDM6B in T cell differentiation (50).

Although not further investigated in our study, we demonstrate that KDM6 inhibition regulates Th1 and Th2 proinflammatory function, supporting a role for KDM6A/B enzymes in immune pathologies, including allergic and respiratory diseases (27, 51). Although H3K27 demethylases KDM6A and KDM6B are constitutively expressed, the cytokine-induced and inflammatory stimulus (such as IL-4, IFN-γ, LPS, and thioglycolate)-induced temporal surge of KDM6B expression in immune cells, including macrophages (52, 53), $CD4^+$ T cells (27), dendritic cells (51), and neutrophils (54), suggests an important epigenetic mechanism in inflammatory scenarios by regulating an early adaptation or response to an inflammatory environment. Our study provides clear evidence that both KDM6 enzymes in humans are important regulatory elements of Th17 cells, by involvement in differentiation of Th17 cells, and in addition by controlling proliferation and proinflammatory effector functions of mature Th17 cells.

Single-cell transcriptomics has provided detailed pictures of cellular heterogeneity related to disease pathology (55), in which Th17 cells exhibit a range of phenotypes from pathogenic to regulatory in nature (56, 57). Our single-cell transcriptomics data indeed show significant T cell heterogeneity, with a consistent set of phenotypes that correlate with subsets of highly inflammatory memory and resting cells. In agreement with our bulk RNA-seq analysis, KDM6 inhibitor treatment of Th17 cells leads to a significant down-regulation in Th17-specific cytokine function and to antiproliferative effects. This is clearly reflected in the single-cell data where significant shifts of highly inflammatory cells following GSK-J4 treatment are observed toward a resting state, suggesting a preferential inhibitor activity on proliferating and inflammatory cells.

Importantly, an effective Th17 cell response requires a T cell to adapt its metabolic state in response to various microenvironments and stimuli. Quiescent T cell energy demands are low, and they primarily oxidize glucose-derived pyruvate in their mitochondria, which ensures optimal ATP production per molecule of glucose (58, 59). Following activation, T cells undergo metabolic reprogramming in order to significantly increase the availability of ATP. These are usually short-lived events that rely primarily on glycolysis for their energy demands (58, 59), which is also observed in cytokine-activated lymphocytes (60). Supporting our observations, the elevated rate of aerobic glycolysis is mirrored by increased expression of nutrient transporters and glycolytic enzymes (61). The increased metabolic flux through the glycolytic pathway is largely regulated by the mTORC1 signaling complex and provides the metabolic precursors necessary for effector functions and proliferation (62). A conspicuous transcriptional response to GSK-J4 treatment, corroborated by knockdown experiments, is a change in metabolic gene expression. Although we observe a characteristic ATF4 signature in NK cells following GSK-J4 treatment (35), we only observe a robust DDIT3 up-regulation in this study with a consistent lack of up-regulated metabolic targets, which are otherwise associated with an ATF4-DDIT3–mediated stress response. Importantly, DDIT3 has been shown to directly repress critical T cell transcription factors like T-bet, leading to reduced cytokine output in tumor-infiltrating T cells and thus might contribute to the observed antiinflammatory phenotype (41).

The observed metabolic changes (i.e., up-regulated glycolytic and down-regulated TCA cycle activity leading to consequent reduction in inflammatory cytokine production and anergy) are best explained by the observed H3K27-mediated silencing of key transcription factors, such as MYC, PPARγ, and PPRC1, as a consequence of GSK-J4 treatment (63). Recently, it has been shown that inhibition of mTORC1 signaling rescues ATF4-deficient cells from MYC-induced endoplasmic reticulum stress (64). This reveals an essential role for ATF4 in survival following MYC activation, and our data suggest that KDM demethylases are an important regulator of this pathway.

We postulate that these mitochondria-centered events (i.e., reduced biogenesis and function, and the TCR-stimulated increase in glycolytic activity) are critical drivers of the observed Th17 phenotype upon demethylase inhibition where anergy is associated with the development of a memory T cell phenotype that leads to down-regulation of glutaminolysis and lipid biosynthesis (65). Importantly, the observed mitochondrial impairment upon demethylase inhibition does not show any sign of stress, such as the mitochondrial unfolded protein response (UPR^{mt}), often associated with a dysfunctional electron transport chain, increased ROS production, and an altered transcription factor, as well as a distinct effector profile (66, 67). Although previous work in *Caenorhabditis elegans* has demonstrated a critical involvement of histone demethylases, including the KDM6B ortholog JMJD3.1, and controlling UPR^{mt} effector regulation, we here do not correlate KDM6B function with a mitochondrial stress response, such as UPR^{mt} (68).

Taken together, our results suggest a critical role of KDM6 enzymes in maintaining Th17 functions by controlling metabolic switches, necessary for T cells to adapt to their specific roles. The results provide a basis for further investigations into using small molecule epigenetic and metabolic inhibitors to understand these critical facets of the adaptive immune system and provide an approach toward therapy.

Materials and Methods

Lymphocyte Isolation. T cells were isolated from venous blood as described for NK cells in ref. 35 and were obtained from healthy volunteers, or from platelet pheresis residues from the Oxford National Health Service Blood Transfusion Service. Peripheral blood was obtained from RA patients attending the rheumatology clinic at Northwick Park Hospital, London whereas peripheral blood samples obtained from AS patients were collected at the Nuffield Orthopedic Centre Hospital, Oxford. The study was approved by the London Riverside Research Ethics Committee (REC) (07/H0706/81) and the Oxford Research Ethics Committee (06/Q1606/139). The research use of human biological samples was in accord with the terms of the patients' informed consents. Patient diagnoses were according to the American College of Rheumatology (ACR) Eular 2010 criteria. Ficoll density gradient centrifugation was applied to obtain mononuclear cells, and $CD4^+$ or $CD45RA^+$ T cells were isolated using magnetic bead isolation using Dynabeads (Invitrogen).

T Helper Cell Differentiation and Enrichment. Differentiation of human $CD4^+$ T cell subsets in vitro was performed as previously described (69–72). In brief, naive $CD4^+$ $CD45RA^+$ T cells were enriched from donor PBMCs using the T cell enrichment kit (Miltenyi). Cell culture was in the presence of anti-CD3/CD28 activation beads (1:20 bead to cell ratio) (Invitrogen) plus

polarization condition medium (RPMI-1640 containing 10% knockout serum replacement [ThermoFisher]) and supplemented with cytokines (vide infra) at 37 °C for 6 d. For Th1 differentiation conditions, naive T cells were cultured in the presence of anti–IL-4 neutralizing antibody (10 mg/mL; R&D) and recombinant human IL-12 (5 ng/mL; R&D). For Th2 conditions, naive T cells were cultured in the presence of anti–IFN-γ neutralizing antibody (10 mg/mL; R&D) in addition to recombinant IL-4 (4 ng/mL; Peprotech). To obtain differentiated Th17 cells, naive T cells were cultured using IL-1β (20 ng/mL; Peprotech), IL-6 (20 ng/mL; Peprotech), recombinant TGF-β (3 ng/mL; Peprotech), and IL-23 (10 ng/mL; R & D) for 7 d. To expand Th17 cells, Dynabeads (Invitrogen) isolated $CD4^+$ T cells were used instead of $CD45RA^+$ selected T cells.

RT-qPCR Analysis. Following total RNA extraction by using TRIzol reagent (Invitrogen) and a Direct-zol RNA Miniprep kit (ZYMO RESEARCH), complementary DNA (cDNA) was generated by using a SuperScript II RT kit (Invitrogen), as per the manufacturer's instructions. Reverse-transcription PCR using specific primers was used to determine the expression levels of each gene. Quantified messenger RNA (mRNA) was normalized to the relative expression of the β-actin gene. All experiments were performed in triplicate. The specific primers used in this study are listed in *SI Appendix*, Table S3.

Compound Inhibitor Screens. Following Th cell differentiation, the cells were seeded at 50,000 cells per well in 200 μL of culture medium in 96-well plates. Compounds were dissolved in DMSO at concentrations previously described in Cribbs et al. (35) and diluted to achieve the desired working solutions. Compound effects were compared with cells cultured in 0.1% DMSO alone whereas wells filled with media served as a background control. Following 24 h of compound treatment, media were harvested, and enzyme-linked immunosorbent assay (ELISA) was used to measure cytokine release. For ISRIB (Sigma) blocking experiments we cultured our cells using 5 nM. Small molecules that were able to modify cytokine expression by a twofold change and $P < 0.05$ were considered as significant.

Locked Nucleic Acid Knockdown Experiments. Knockdown experiments using locked nucleic acid (LNA) antisense oligonucleotides were designed and synthesized as previously described (73). LNAs were synthesized by Santaris A/S (now Roche Innovation Centre Copenhagen). Following synthesis, LNAs were HPLC-purified and desalted using a Milliprep membrane, and the resulting mass was verified by LC-MS. T helper cells were cultured at a concentration of 1×10^6 cells per milliliter and then stimulated with IL-15. LNAs were added to the culture medium using a final concentration of 1 μM, followed by culture for 8 d.

ELISA. ELISA (eBioscience) was used to measure the concentration of IFN-γ, IL17, and IL-4 cytokines within the cell culture supernatant, which was performed according to the manufacturer's instructions. Standards and samples were measured in triplicate.

Chromatin Immunoprecipitation Followed by Sequencing. Chromatin immunoprecipitation (ChIP) was performed as previously described (35, 74). All ChIP-seq assays were performed using single donors in triplicate. For quantitative ChIP-seq experiments, 4×10^6 SF9 cells were spiked into the pool. The cells were treated with formaldehyde to cross-link, and chromatin was fragmented to 200 to 300 bp, using a Biorupter Pico sonicator (Diagenode). Each lysate was immunoprecipitated with 10 μg of anti-H3K4me3 (Merck Millipore) and anti-H3K27me3 (Merck Millipore) antibodies. The chromatin immunoprecipitation (ChIP) experiment was then performed for each antibody as described previously by Orlando et al. (74). Library preparation was performed using a NEBNext Ultra DNA sample preparation kit (NEB), according to the manufacturer's recommendations. The samples were multiplexed, quantified using a High-sensitivity d1000 TapeStation (Agilent) or a Kapa library quantification kit (KAPA Biosystems), and then sequenced using a NextSeq 500 (Illumina) (paired-end, 2×41 bp). Sequencing depth was >20 million reads per sample.

Flow Cytometry. For flow cytometry detection of surface molecules, T cells were first incubated with anti-Fc receptor antibody (Ab), to reduce nonspecific binding, and then labeled with appropriate fluorescent monoclonal antibodies (mAbs). For intracellular staining of cytokines, T cells were stimulated with phorbol 12-myristate 13-acetate (50 ng/mL) and ionomycin (1 mg/mL) for 4 h in the presence of protein transport inhibitor solution (WHICH ONE). The cells were collected, washed, fixed, permeabilized (fix/perm; Biolegend), and stained with fluorescein-labeled cytokine-specific mAbs according to the manufacturer's instructions. Appropriate fluorescein-conjugated, isotype-matched mAbs were used as negative controls. Flow cytometry antibodies used in this study are detailed in the key resources table (*SI Appendix*, Table S1). Cells were then analyzed using a BD Fortessa flow cytometry instrument.

RNA Isolation and Bulk RNA-Seq Library Preparation. RNA was isolated from isolated T cells using a Quick-RNA MiniPrep kit (Zymo), following the manufacturer's recommendations. The quality of the RNA samples was verified using an RNA screen tape on a TapeStation (Agilent). The RIN values for all samples were >7.5. Libraries were prepared using the NEBNext Ultra RNA library prep kit using TruSeq indexes, following the manufacturer's recommendations. The resulting libraries were sequenced on a NextSeq 500 platform (Illumina) using a paired-end run (2×41 bp).

Single-Cell RNA-Seq Library Preparation. Single-cell capture and reverse transcription (RT) were performed as previously described (75). Cells were loaded into a microfluidics cartridge at a concentration of 310 cells per microliter. Cell capture, lysis, and reverse transcription were all performed using a Nadia instrument (Dolomite Bio). RT reactions were performed using ChemGene beads also captured in the microfluidic wells. Beads were collected from the device, and then cDNA amplification was performed. Prior to PCR, the beads were treated with Exo-I. Following PCR, purified cDNA was used as an input for Nextera tagmentation reactions. cDNA library quality was assessed using a TapeStation (Agilent Technologies). All cDNA purification steps were performed using Ampure XP beads (Beckman). High quality samples were then sequenced on a NextSeq 500 sequencer using a 75-cycle High Output kit (Illumina).

Metabolomic Studies. Naive $CD4^+$ T cells were isolated from six human donors and subdivided into eight equal groups: baseline (predifferentiation, undifferentiated T cells), Th17 differentiated T cells (postdifferentiation), Th17 differentiated cells treated with vehicle (DMSO), GSK-J4 or GSK-J5 (2 μM each in 0.1% DMSO final concentration) for both 12 and 24 h. Following each treatment, T cells were isolated, pelleted, and snap-frozen for further global, unbiased metabolomic analysis on the HD4 accurate mass platform (76). In addition, media samples were collected for predifferentiation, postdifferentiation, and 24-h samples treated with DMSO, GSK-J4, and GSK-J5.

Mitochondrial Function. T cells were stained with 20 μM CM-H_2DCFDA and 200 nM or 100 nM TMRE in phosphate-buffered saline (PBS) for 30 min at 37 °C (5% CO_2) to determine ROS production and mitochondrial membrane potential, respectively. After staining, cells were washed with PBS, and fluorescence was measured using a Beckman Coulter CytoFLEX flow cytometer.

Bulk RNA Sequencing Analysis. A computational pipeline was written calling scripts from the CGAT toolkit (77, 78) (https://github.com/cgat-developers/cgat-flow). Sequencing reads were mapped to the human genome GRCh37 (hg19) assembly using hisat v0.1.6 (79). Reads were mapped to genes using featureCounts v1.4.6 (part of the subreads package) (80) where only uniquely mapped reads were used in the counting step. A counts table was generated and used for differential expression analysis, performed using DESeq2 v1.12.3 within the R statistical framework v3.3.0 (81). R scripts used for transcriptomic data analysis are available through GitHub (https://github.com/Acribbs/deseq2_report). A level of ±2-fold change and a false discovery rate of <0.05 were used as threshold to define significantly regulated genes.

Single-Cell RNA Sequencing Analysis. Reads were demultiplexed, aligned to the GRCh37 (hg19) assembly reference genome, and filtered; and cell barcodes and unique molecular identifiers (UMIs) were quantified using dropseq tools (75). Dropseq tools uses STAR (80) for alignment. For each gene, UMI counts of all transcript isoforms were summed to obtain a digital measure of total gene expression. All further filtering was performed with Seurat v2.1 (82). Following filtering we were able to detect 1,998 cells treated with DMSO and 1,962 cells treated with GSK-J4. Of these cells, 2,835 median number of genes were detected, with 430 genes expressed in at least 50% of cells. Briefly, outliers were detected for each quality metric that included cells that expressed a minimum of 50 genes per cell and a mitochondrial content of less than 5%.

Dimensionality Reduction and Clustering. Full descriptions on the clustering procedure can be found in the *monocle2* documentation. Briefly, after QC and filtering, gene expression for each cell was normalized by total transcript count and log transformed. To identify highly variable genes that

account for cellular heterogeneity, covarying genes were reduced using the tSNE reduction method. For unbiased clustering, *monocle2* uses density peak clustering. Clusters were then projected onto a tSNE plot. Cluster identification was robust across a range of PCs and resolutions.

Pseudotime Ordering. Pseudotime ordering was performed using the *monocle* package (v2.11.3) to isolate a set of ordering genes that define the progression of T cell activation, using the GO term "T cell activation" (GO:0042110) (83). Next, we reduced data dimensionality using the *DDRTree* method and ordered cells along the resulting trajectory. Finally, we identified genes that change as a function of the computed pseudotime using the *differentialGeneTest* function. A *q*-value threshold of 0.01 was applied to all differential expression tests in the *monocle* workflow. Gene expression heat maps were produced using the *pheatmap* package (v1.0.12).

Differential Gene Expression. Differentially expressed gene analysis was performed using the nonparametric Wilcoxon test on $\log_2$(TPM) expression values for the comparison of expression level and Fisher's exact test for the comparison of expressing cell frequency. *P* values generated from both tests were then combined using Fisher's method and were adjusted using Benjamini–Hochberg (BH). Differentially expressed genes were selected on the basis of the absolute $\log_2$ fold change of ≥ 1 and the adjusted *P* value of < 0.05. Selected genes were subjected to the hierarchical clustering analysis using Pearson correlation as a distance, with clustering performed in R.

ChIP and Assay for Transposase-Accessible Chromatin Sequencing Analysis. Bowtie software v0.12.5 was used to map reads to the human genome GRCh37 (hg19) assembly (84). Reads were only reported that were aligned to the genome, accounting for up to two mismatches. For quantitative ChIP, reads mapping to SF9 cells were determined for each sample and used as a scaling factor, as previously described by Orlando et al. (74). Bedtools v2.2.24 was used to create bedgraph files from the mapped BAM files, and averaged tracks for each condition were produced, representing the mean of the scaled values for biological replicates. Homer tag directories were then generated using the raw read function, and TSS coverage plots were plotted in R. MACS software (v1.4.2) was used to identify enrichment of intervals of H3K4me3 and H3K27me3 following ChIP-seq and regions of open chromatin following assay for transposase-accessible chromatin sequencing (ATAC-seq). Sequencing of the whole cell extract was performed to determine the background model when analyzing ChIP-seq

Metabolomic Analysis. Welch's two-sample *t* tests, repeated measures ANOVA, and random forest analysis were used to analyze the data. For all analyses, following normalization to protein for cells, missing values, if any, were imputed with the observed minimum for that particular compound. The statistical analyses were performed on natural log-transformed data (see Dataset S3). When comparing GSK-J4– or GSK-J5–treated cells with time-matched DMSO controls using Student *t* tests, it became clear that a donor effect was limiting in terms of understanding the true drug-related changes. Hence, repeated measures ANOVA was used to compare each donor response to drug with its own DMSO control, thereby addressing the donor effect and revealing the true drug response profiles within this study (Dataset S3).

Mass Cytometry Analysis. For each sample, 1 to 3 million cells were first stained with a solution containing rhodium DNA intercalator (Fluidigm) to distinguish live/dead and IdU (Fluidigm) to distinguish cells in S-phase, prior to Fc receptor blocking (Miltenyi Biotec). Samples were then stained with a mixture of metal-conjugated antibodies recognizing cell surface antigens (all antibodies purchased from Fluidigm) (*SI Appendix*, Table S1). After washing in Maxpar cell-staining buffer (Fluidigm), samples were fixed in ice cold methanol for 15 min prior to washing and incubation with metal-conjugated antibodies recognizing intracellular and phospho-protein antigens. Samples were washed twice in cell-staining buffer, fixed by incubation with 1.6% PFA (Pierce) for 10 min, and finally incubated overnight with iridium DNA intercalator in Maxpar fix and perm buffer (Fluidigm). Prior to acquisition, samples were washed twice in Maxpar cell-staining buffer and twice in Maxpar water and filtered through a 40-μm cell strainer before being acquired on a Helios mass cytometer (Fluidigm).

After acquisition, all .fcs files in the experiment were normalized using tools within the Helios software and then uploaded to Cytobank (https://www.cytobank.org/) for all gating and further analysis, including using clustering and dimensionality reduction algorithms such as SPADE and viSNE (85).

Statistical Analysis. All other statistical analyses were performed with GraphPad Prism7 software. Unless indicated otherwise, data are expressed as mean ± standard deviation (SD). For multiple group comparison, the one-way analysis of variance (ANOVA) was used, followed by the Dunnett's test for multiple correction. A paired Student's *t* test was used for single comparisons. Statistical tests were chosen prior to determining if the data followed a Gaussian distribution (using D'Agostino and Pearson test).

Data and Software Availability. Single-cell RNA-seq, RNA-seq, ATAC-seq, and ChIP-seq datasets are deposited with the GEO database under accession number GSE127767. A computational pipeline was written employing scripts from the CGAT toolkit (84, 86) to analyze the next generation sequencing data (https://github.com/cgat-developers/cgat-flow). R scripts used for transcriptomic data analysis are available through GitHub (https://github.com/Acribbs/deseq2_report). Our single-cell data was analyzed using workflows available through GitHub (https://github.com/Acribbs/scflow).

ACKNOWLEDGMENTS. The study was supported through funding from the Kennedy Trust for Rheumatology Research, Arthritis Research UK (Program Grant 20522), the National Institute for Health Research Oxford Biomedical Research Unit, Cancer Research UK (CRUK), and a Leducq Epigenetics of Atherosclerosis Network program grant from the Leducq Foundation. M.d.W. is supported by grants from the Netherlands Heart Foundation (GENIUS2), the Netherlands Heart Foundation and Spark Holland (2015B002), and the European Union (Initial Training Networks Grant EPIMAC). A.P.C. was supported by the Medical Research Council (MRC) CGAT program (G1000902) and a CRUK Oxford Centre Development Fund award (CRUKDF-0318-AC[AZ]). The Structural Genomics Consortium is a registered charity (1097737) that receives funds from Abbvie, Bayer Healthcare, Boehringer Ingelheim, the Canadian Institutes for Health Research, the Canadian Foundation for Innovation, Eli Lilly and Company, Genome Canada, the Ontario Ministry of Economic Development and Innovation, Janssen, the Novartis Research Foundation, Pfizer, Takeda, and the Wellcome Trust. The research leading to these results has received funding from the People Programme (Marie Curie Actions) (to U.O.) of the European Union's Seventh Framework Programme (FP7/2007-2013) under Research Executive Agency Grant Agreement 609305.

1. I. Sandquist, J. Kolls, Update on regulation and effector functions of Th17 cells. *F1000 Res.* **7**, 205 (2018).
2. T. Korn, E. Bettelli, M. Oukka, V. K. Kuchroo, IL-17 and Th17 cells. *Annu. Rev. Immunol.* **27**, 485–517 (2009).
3. C. Dong, TH17 cells in development: An updated view of their molecular identity and genetic programming. *Nat. Rev. Immunol.* **8**, 337–348 (2008).
4. S. L. Gaffen, R. Jain, A. V. Garg, D. J. Cua, The IL-23-IL-17 immune axis: From mechanisms to therapeutic testing. *Nat. Rev. Immunol.* **14**, 585–600 (2014).
5. A. Akitsu, Y. Iwakura, Interleukin-17-producing γδ T (γδ17) cells in inflammatory diseases. *Immunology* **155**, 418–426 (2018).
6. E. Bettelli *et al.*, Reciprocal developmental pathways for the generation of pathogenic effector TH17 and regulatory T cells. *Nature* **441**, 235–238 (2006).
7. P. R. Mangan *et al.*, Transforming growth factor-beta induces development of the T(H)17 lineage. *Nature* **441**, 231–234 (2006).
8. M. Veldhoen, R. J. Hocking, C. J. Atkins, R. M. Locksley, B. Stockinger, TGFbeta in the context of an inflammatory cytokine milieu supports de novo differentiation of IL-17-producing T cells. *Immunity* **24**, 179–189 (2006).
9. T. Korn *et al.*, IL-21 initiates an alternative pathway to induce proinflammatory T(H)17 cells. *Nature* **448**, 484–487 (2007).
10. Y. Chung *et al.*, Critical regulation of early Th17 cell differentiation by interleukin-1 signaling. *Immunity* **30**, 576–587 (2009).
11. D. J. Cua *et al.*, Interleukin-23 rather than interleukin-12 is the critical cytokine for autoimmune inflammation of the brain. *Nature* **421**, 744–748 (2003).
12. I. I. Ivanov *et al.*, The orphan nuclear receptor RORgammat directs the differentiation program of proinflammatory IL-17+ T helper cells. *Cell* **126**, 1121–1133 (2006).
13. M. H. Al-Mossawi *et al.*, THU0503 in-vitro supression of TH17 responses in inflammatory arthritis patients using small molecule ror-gamma-T Inhibitors. *Ann. Rheum. Dis.* **73**, 357 (2014).
14. J. R. Huh, D. R. Littman, Small molecule inhibitors of RORγt: Targeting Th17 cells and other applications. *Eur. J. Immunol.* **42**, 2232–2237 (2012).
15. J. Skepner *et al.*, Pharmacologic inhibition of RORγt regulates Th17 signature gene expression and suppresses cutaneous inflammation in vivo. *J. Immunol.* **192**, 2564–2575 (2014).
16. K. Hirahara *et al.*, Helper T-cell differentiation and plasticity: Insights from epigenetics. *Immunology* **134**, 235–245 (2011).
17. P. Durek *et al.*; DEEP Consortium, Epigenomic profiling of human $CD4^+$ T cells supports a linear differentiation model and highlights molecular regulators of memory development. *Immunity* **45**, 1148–1161 (2016).
18. T. Jenuwein, C. D. Allis, Translating the histone code. *Science* **293**, 1074–1080 (2001).
19. E. L. Greer, Y. Shi, Histone methylation: A dynamic mark in health, disease and inheritance. *Nat. Rev. Genet.* **13**, 343–357 (2012).

20. K. Ichiyama *et al*., The methylcytosine dioxygenase Tet2 promotes DNA demethylation and activation of cytokine gene expression in T cells. *Immunity* **42**, 613–626 (2015).
21. Y. Wei *et al*., Global H3K4me3 genome mapping reveals alterations of innate immunity signaling and overexpression of JMJD3 in human myelodysplastic syndrome CD34+ cells. *Leukemia* **27**, 2177–2186 (2013).
22. C. J. Cohen *et al*., Human Th1 and Th17 cells exhibit epigenetic stability at signature cytokine and transcription factor loci. *J. Immunol.* **187**, 5615–5626 (2011).
23. G. Wei *et al*., Global mapping of H3K4me3 and H3K27me3 reveals specificity and plasticity in lineage fate determination of differentiating CD4+ T cells. *Immunity* **30**, 155–167 (2009).
24. A. Hammitzsch *et al*., CBP30, a selective CBP/p300 bromodomain inhibitor, suppresses human Th17 responses. *Proc. Natl. Acad. Sci. U.S.A.* **112**, 10768–10773 (2015).
25. D. A. Mele *et al*., BET bromodomain inhibition suppresses TH17-mediated pathology. *J. Exp. Med.* **210**, 2181–2190 (2013).
26. Z. Liu *et al*., The histone H3 lysine-27 demethylase Jmjd3 plays a critical role in specific regulation of Th17 cell differentiation. *J. Mol. Cell Biol.* **7**, 505–516 (2015).
27. Q. Li *et al*., Critical role of histone demethylase Jmjd3 in the regulation of CD4+ T-cell differentiation. *Nat. Commun.* **5**, 5780 (2014).
28. K. E. Wellen, C. B. Thompson, A two-way street: Reciprocal regulation of metabolism and signalling. *Nat. Rev. Mol. Cell Biol.* **13**, 270–276 (2012).
29. C. Lu, C. B. Thompson, Metabolic regulation of epigenetics. *Cell Metab.* **16**, 9–17 (2012).
30. W. G. Kaelin, Jr, S. L. McKnight, Influence of metabolism on epigenetics and disease. *Cell* **153**, 56–69 (2013).
31. R. P. Nowak *et al*., Advances and challenges in understanding histone demethylase biology. *Curr. Opin. Chem. Biol.* **33**, 151–159 (2016).
32. T. Xu *et al*., Metabolic control of T_H17 and induced T_{reg} cell balance by an epigenetic mechanism. *Nature* **548**, 228–233 (2017).
33. K. B. Shpargel, J. Starmer, D. Yee, M. Pohlers, T. Magnuson, KDM6 demethylase independent loss of histone H3 lysine 27 trimethylation during early embryonic development. *PLoS Genet.* **10**, e1004507 (2014).
34. S. Manna *et al*., Histone H3 Lysine 27 demethylases Jmjd3 and Utx are required for T-cell differentiation. *Nat. Commun.* **6**, 8152 (2015).
35. A. Cribbs *et al*., Inhibition of histone H3K27 demethylases selectively modulates inflammatory phenotypes of natural killer cells. *J. Biol. Chem.* **293**, 2422–2437 (2018).
36. L. Kruidenier *et al*., A selective jumonji H3K27 demethylase inhibitor modulates the proinflammatory macrophage response. *Nature* **488**, 404–408 (2012).
37. B. Heinemann *et al*., Inhibition of demethylases by GSK-J1/J4. *Nature* **514**, E1–E2 (2014).
38. T. Satoh *et al*., The Jmjd3-Irf4 axis regulates M2 macrophage polarization and host responses against helminth infection. *Nat. Immunol.* **11**, 936–944 (2010).
39. C. Doñas *et al*., The histone demethylase inhibitor GSK-J4 limits inflammation through the induction of a tolerogenic phenotype on DCs. *J. Autoimmun.* **75**, 105–117 (2016).
40. C. Sidrauski, A. M. McGeachy, N. T. Ingolia, P. Walter, The small molecule ISRIB reverses the effects of eIF2α phosphorylation on translation and stress granule assembly. *eLife* **4**, e05033 (2015).
41. Y. Cao *et al*., ER stress-induced mediator C/EBP homologous protein thwarts effector T cell activity in tumors through T-bet repression. *Nat. Commun.* **10**, 1280 (2019).
42. C. Trapnell *et al*., The dynamics and regulators of cell fate decisions are revealed by pseudotemporal ordering of single cells. *Nat. Biotechnol.* **32**, 381–386 (2014).
43. V. A. Gerriets *et al*., Metabolic programming and PDHK1 control CD4+ T cell subsets and inflammation. *J. Clin. Invest.* **125**, 194–207 (2015).
44. M. A. Qureshi, C. M. Haynes, M. W. Pellegrino, The mitochondrial unfolded protein response: Signaling from the powerhouse. *J. Biol. Chem.* **292**, 13500–13506 (2017).
45. C. Naruse *et al*., New insights into the role of Jmjd3 and Utx in axial skeletal formation in mice. *FASEB J.* **31**, 2252–2266 (2017).
46. J. S. Burchfield, Q. Li, H. Y. Wang, R. F. Wang, JMJD3 as an epigenetic regulator in development and disease. *Int. J. Biochem. Cell Biol.* **67**, 148–157 (2015).
47. G. G. Welstead *et al*., X-linked H3K27me3 demethylase Utx is required for embryonic development in a sex-specific manner. *Proc. Natl. Acad. Sci. U.S.A.* **109**, 13004–13009 (2012).
48. T. Burgold *et al*., The H3K27 demethylase JMJD3 is required for maintenance of the embryonic respiratory neuronal network, neonatal breathing, and survival. *Cell Rep.* **2**, 1244–1258 (2012).
49. Y. Jiang *et al*., Epigenetic activation during T helper 17 cell differentiation is mediated by Tripartite motif containing 28. *Nat. Commun.* **9**, 1424 (2018).
50. S. A. Miller, S. E. Mohn, A. S. Weinmann, Jmjd3 and UTX play a demethylase-independent role in chromatin remodeling to regulate T-box family member-dependent gene expression. *Mol. Cell* **40**, 594–605 (2010).
51. C. A. Malinczak *et al*., Upregulation of H3K27 demethylase KDM6 during respiratory syncytial virus infection enhances proinflammatory responses and immunopathology. *J. Immunol.* **204**, 159–168 (2020).
52. F. De Santa *et al*., The histone H3 lysine-27 demethylase Jmjd3 links inflammation to inhibition of polycomb-mediated gene silencing. *Cell* **130**, 1083–1094 (2007).
53. M. Ishii *et al*., Epigenetic regulation of the alternatively activated macrophage phenotype. *Blood* **114**, 3244–3254 (2009).
54. J. A. Ericson *et al*.; ImmGen Consortium, Gene expression during the generation and activation of mouse neutrophils: Implication of novel functional and regulatory pathways. *PLoS One* **9**, e108553 (2014).
55. V. Proserpio, B. Mahata, Single-cell technologies to study the immune system. *Immunology* **147**, 133–140 (2016).
56. J. T. Gaublomme *et al*., Single-cell genomics unveils critical regulators of Th17 cell pathogenicity. *Cell* **163**, 1400–1412 (2015).
57. C. Wang *et al*., CD5L/AIM regulates lipid biosynthesis and restrains Th17 cell pathogenicity. *Cell* **163**, 1413–1427 (2015).
58. R. Wang *et al*., The transcription factor Myc controls metabolic reprogramming upon T lymphocyte activation. *Immunity* **35**, 871–882 (2011).
59. C. J. Fox, P. S. Hammerman, C. B. Thompson, Fuel feeds function: Energy metabolism and the T-cell response. *Nat. Rev. Immunol.* **5**, 844–852 (2005).
60. E. L. Pearce, E. J. Pearce, Metabolic pathways in immune cell activation and quiescence. *Immunity* **38**, 633–643 (2013).
61. R. P. Donnelly *et al*., mTORC1-dependent metabolic reprogramming is a prerequisite for NK cell effector function. *J. Immunol.* **193**, 4477–4484 (2014).
62. S. Nagai, Y. Kurebayashi, S. Koyasu, Role of PI3K/Akt and mTOR complexes in Th17 cell differentiation. *Ann. N. Y. Acad. Sci.* **1280**, 30–34 (2013).
63. L. Franchi *et al*., Inhibiting oxidative phosphorylation in vivo restrains Th17 effector responses and ameliorates murine colitis. *J. Immunol.* **198**, 2735–2746 (2017).
64. F. Tameire *et al*., ATF4 couples MYC-dependent translational activity to bioenergetic demands during tumour progression. *Nat. Cell Biol.* **21**, 889–899 (2019).
65. K. P. Hough, D. A. Chisolm, A. S. Weinmann, Transcriptional regulation of T cell metabolism. *Mol. Immunol.* **68**, 520–526 (2015).
66. S. Callegari, S. Dennerlein, Sensing the stress: A role for the UPR^{mt} and UPR^{am} in the quality control of mitochondria. *Front. Cell Dev. Biol.* **6**, 31 (2018).
67. P. M. Quirós *et al*., Multi-omics analysis identifies ATF4 as a key regulator of the mitochondrial stress response in mammals. *J. Cell Biol.* **216**, 2027–2045 (2017).
68. C. Merkwirth *et al*., Two conserved histone demethylases regulate mitochondrial stress-induced longevity. *Cell* **165**, 1209–1223 (2016).
69. E. V. Acosta-Rodriguez, G. Napolitani, A. Lanzavecchia, F. Sallusto, Interleukins 1beta and 6 but not transforming growth factor-beta are essential for the differentiation of interleukin 17-producing human T helper cells. *Nat. Immunol.* **8**, 942–949 (2007).
70. S. Nakae, Y. Iwakura, H. Suto, S. J. Galli, Phenotypic differences between Th1 and Th17 cells and negative regulation of Th1 cell differentiation by IL-17. *J. Leukoc. Biol.* **81**, 1258–1268 (2007).
71. T. Sornasse, P. V. Larenas, K. A. Davis, J. E. de Vries, H. Yssel, Differentiation and stability of T helper 1 and 2 cells derived from naive human neonatal CD4+ T cells, analyzed at the single-cell level. *J. Exp. Med.* **184**, 473–483 (1996).
72. L. Li *et al*., TLR8-mediated metabolic control of human Treg function: A mechanistic target for cancer immunotherapy. *Cell Metab.* **29**, 103–123.e5 (2019).
73. C. A. Stein *et al*., Efficient gene silencing by delivery of locked nucleic acid antisense oligonucleotides, unassisted by transfection reagents. *Nucleic Acids Res.* **38**, e3 (2010).
74. D. A. Orlando *et al*., Quantitative ChIP-Seq normalization reveals global modulation of the epigenome. *Cell Rep.* **9**, 1163–1170 (2014).
75. E. Z. Macosko *et al*., Highly parallel genome-wide expression profiling of individual cells using nanoliter droplets. *Cell* **161**, 1202–1214 (2015).
76. A. M. Evans *et al*., High resolution mass spectrometry improves data quantity and quality as compared to unit mass resolution mass spectrometry in high- throughput profiling metabolomics. *Metabolomics* **4**, 132 (2014).
77. D. Kim, B. Langmead, S. L. Salzberg, HISAT: A fast spliced aligner with low memory requirements. *Nat. Methods* **12**, 357–360 (2015).
78. Y. Liao, G. K. Smyth, W. Shi, featureCounts: An efficient general purpose program for assigning sequence reads to genomic features. *Bioinformatics* **30**, 923–930 (2014).
79. M. I. Love, W. Huber, S. Anders, Moderated estimation of fold change and dispersion for RNA-seq data with DESeq2. *Genome Biol.* **15**, 550 (2014).
80. A. Dobin *et al*., STAR: Ultrafast universal RNA-seq aligner. *Bioinformatics* **29**, 15–21 (2013).
81. B. Langmead, C. Trapnell, M. Pop, S. L. Salzberg, Ultrafast and memory-efficient alignment of short DNA sequences to the human genome. *Genome Biol.* **10**, R25 (2009).
82. A. Butler, P. Hoffman, P. Smibert, E. Papalexi, R. Satija, Integrating single-cell transcriptomic data across different conditions, technologies, and species. *Nat. Biotechnol.* **36**, 411–420 (2018).
83. C. Trapnell *et al*., The dynamics and regulators of cell fate decisions are revealed by pseudotemporal ordering of single cells. *Nat. Biotechnol.* **32**, 381–386 (2014).
84. D. Sims *et al*., CGAT: Computational genomics analysis toolkit. *Bioinformatics* **30**, 1290–1291 (2014).
85. A. D. Amir *et al*., viSNE enables visualization of high dimensional single-cell data and reveals phenotypic heterogeneity of leukemia. *Nat. Biotechnol.* **31**, 545–552 (2013).
86. A. P. Cribbs *et al*., CGAT-core: A python framework for building scalable, reproducible computational biology workflows. *F1000 Res.* **8**, 377 (2019).